RESEARCH ARTICLE

How organized is deep convection over Germany?

Ieda Pscheidt[1] | Fabian Senf[2] | Rieke Heinze[3] | Hartwig Deneke[2] | Silke Trömel[1] |
Cathy Hohenegger[3]

[1]Institute for Geosciences and Meteorology, University of Bonn, Bonn, Germany

[2]Remote Sensing of Atmospheric Processes, Leibniz Institute for Tropospheric Research, Leipzig, Germany

[3]Max Planck Institute for Meteorology, Hamburg, Germany

Correspondence
Ieda Pscheidt, Institute for Geosciences and Meteorology, University of Bonn, Auf dem Hügel 20, 53121 Bonn, Germany.
Email: pscheidt@uni-bonn.de

Abstract
Deep moist convection shows a tendency to organize into mesoscale structures. To be able to understand the potential effect of convective organization on the climate, one needs first to characterize organization. In this study, we systematically characterize the organizational state of convection over Germany based on two years of cloud-top observations derived from the Meteosat Second Generation satellite and of precipitation cores detected by the German C-band radar network. The organizational state of convection is characterized by commonly employed organization indices, which are mostly based on the object numbers, sizes and nearest-neighbour distances. According to the organization index I_{org}, cloud tops and precipitation cores are found to be in an organized state for 69% and 92% of the time, respectively. There is an increase in rainfall when the number of objects and their sizes increase, independently of the organizational state. Case-studies of specific days suggest that convectively organized states correspond to either local multi-cell clusters, with less numerous, larger objects close to each other, or to scattered clusters, with more numerous, smaller organized objects spread out over the domain. For those days, simulations are performed with the large-eddy model ICON with grid spacings of 625, 312 and 156 m. Although the model underestimates rainfall and shows a too large cold cloud coverage, the organizational state is reasonably well represented without significant differences between the grid spacings.

KEYWORDS
convective organization, ICON model, organization indices, model evaluation

1 | INTRODUCTION

Convective clouds can be observed in very different organizational states – organized, random or regular. The diversity of organizational states ranges from small-scale structures up to large cloud systems that organize in squall lines, in non-squall clusters or even in planetary-scale cloud envelopes (Houze and Betts, 1981; Holloway *et al.*, 2017). For decades, the question has been discussed of whether convection has a

preference for a specific organizational state. Organization of clouds in clusters seems to be facilitated by diverse forcings like wind shear, cloud interactions due to local moistening of the environment, or evaporation of rainwater in the sub-cloud layer that fuels cold pools, to mention a few (Randall and Huffman, 1980; van Delden and Oerlemans, 1982; Nakajima and Matsuno, 1988; Mapes *et al.*, 2006). In contrast, strong subsidence in the vicinity of already formed clouds, the decrease in the available convective potential energy in the

nearby environment, changes in near-cloud atmospheric stability and circulation feedbacks lead to a regularly distributed state. (Houze and Betts, 1981; Bretherton, 1988; Ramirez and Bras, 1990; Ramirez *et al.*, 1990). Different organizational states seem also to depend on the stage of the cloud life cycle with a tendency towards organization in the early stages of the cloud growth and in the dissipation phase, and a change towards either random or regular distribution in the mature stage (Nair *et al.*, 1998).

Diverse studies have investigated the impact of convective organizations on the mean state of the atmosphere (Holloway *et al.*, 2017; Wing *et al.*, 2017 give recent reviews). In the last 30 years the regional increase of rainfall over the Tropics has been attributed to the increase in the frequency of convective organization (Tselioudis *et al.*, 2010; Tan *et al.*, 2010). In idealized simulations conducted for the same region, the vertical profile of heating appears strongly modified by the development of cloud clusters (Houze, 1981; Tselioudis *et al.*, 2010). Also, changes in the diabatic heating can modify the average large-scale atmospheric circulation (Hartmann *et al.*, 1984) and feedbacks between convective organization and large-scale atmospheric state might ultimately impact the large-scale dynamics and the transport of water and energy (Tobin *et al.*, 2012).

Recently, idealized convection-permitting model simulations have shown that convection may spontaneously organize into large cloud clusters leading to a drier free troposphere, to more outgoing long-wave radiation and to shrinking of the upper-tropospheric cloud amounts (Bretherton *et al.*, 2005; Bony *et al.*, 2015; Wing and Cronin, 2016; Holloway and Woolnough, 2016). This drew the attention of the scientific community to the questions:
(a) can convective organizations lead to a negative climate feedback? and
(b) how does the inability of current climate prediction models to explicitly resolve mesoscale organization (Moncrieff and Liu, 2006; Moncrieff, 2010) affect the prediction of future climate scenarios?

Motivated by the need of a thorough understanding of convective organization, one needs first to be able to characterize them. Previous studies have investigated convective organization in observations from either radar (e.g. Lopez, 1978; Cheng *et al.*, 2018) or satellite (e.g. Ramirez and Bras, 1990; Zhu *et al.*, 1992; Nair *et al.*, 1998; Tobin *et al.*, 2012; White *et al.*, 2018). However, we now systematically identify the organizational state of convective clouds by using both radar and satellite observations. We adopt commonly used organization indices to provide a first climatology of organization over Germany. In addition, we also evaluate convective organization in large-eddy model simulations to understand the effect of the model's grid spacing on the representation of organization. To that end, simulations conducted for selected days are evaluated by means of the organization indices.

The following section presents the observations, the model set-up and the selected cases of convection for model simulation. Section 3 describes a threshold-based segmentation algorithm for the detection of convective clouds needed for computing the organization indices as well as the organization indices themselves. Section 4 provides the climatology of organization indices and hence, of the organizational states, as well as the evaluation of the model's performance. Summary and conclusions are provided in Section 5.

2 | DATA AND FRAMEWORK

We identify signatures of convective clouds for the extended summer seasons (April to September) of the years 2014 and 2015. Strong signals in radar reflectivities, which are associated with heavy rainfall, and low satellite brightness temperatures (BTs) that indicate higher cloud tops are used as proxies of convection and/or convective clouds. These datasets are described in details in Section 2.1. The model simulations are performed with the ICOsahedral Non-hydrostatic (ICON) model in large-eddy simulation (LES) mode (Dipankar *et al.*, 2015; Heinze *et al.*, 2017), called ICON-LEM, with grid spacings of 625, 312, and 156 m. An overview of the synoptic situation for the selected simulated cases is given in Section 2.2 and the model configuration is described in Section 2.3. Section 2.4 provides a description of the model-derived radar and satellite data for model evaluation.

2.1 | Observations

We use RX- and RY-Radolan composites based on measurements from up to 16 Doppler C-band radars covering Germany and operated by the German Weather Service (DWD) (Bartels *et al.*, 2004). The RX product is a 2D mosaic of the radar reflectivity based on the terrain-following precipitation scan. The dataset is provided by the DWD in a 900 km × 900 km grid with 1 km × 1 km resolution and is available every 5 min. The RY composite is the rainfall rate 2D mosaic obtained from the reflectivity after correction of orographic attenuation effects and the application of a variable Z–R relationship based on precipitation type (Bartels *et al.*, 2004; Weigl, 2015; DWD, 2018). The spatio-temporal resolution is the same as in RX. Note, however, that although the German radar network has a good density and Radolan provides 1 km × 1 km products, the original observations have in many places a different spatial resolution. Due to the fact that each radar measures with a 1° beamwidth, the original radar observations have a beamwidth of around 1 km at 60 km distance from each radar site (through simple considerations with $2\pi r/360$, where r is the range). Therefore, the original radar measurements in many places have either a finer (range <60 km) or a coarser (range >60 km) resolution than the Radolan products.

In addition to observations related to surface rainfall, we utilize cloud-top observations from the Spinning Enhanced Visible and Infrared Imager (SEVIRI) aboard geostationary Meteosat Second Generation (MSG) satellites operated by EUMETSAT (Schmetz *et al.*, 2002). The analysis only considers information from the infrared window channel with a central wavelength of 10.8 μm (similar to the study by Rempel *et al.* (2017)). This channel is located in the atmospheric window region and is only slightly influenced by the absorption of atmospheric gases (Schmetz *et al.*, 2002). Radiance measured at 10.8 μm is converted into equivalent black body temperature, i.e. the BT. The observed BTs give a measure of the temperature at the cloud-top level for optically thick clouds. For semi-transparent cirrus clouds, BTs become warmer than the corresponding cloud-top temperature and include contributions from the atmosphere and clouds below as well as from the surface. Compared to the radar data, the infrared observations of MSG SEVIRI have a much coarser spatial resolution of roughly 4 km × 6 km over the studied domain and are available every 15 min.

For the purpose of this study we use the RX, RY and BT datasets with 30 min time step (0000, 0030, 0100, 0130, ..., 2330 UTC). Furthermore, we interpolate them with the nearest-neighbour method to a grid of approximately 1.2 km spacing (hereinafter referred to as a grid cell). This is the same grid cell of the remapped outputs of the ICON simulations used in this study and described in Section 2.3.

2.2 | Synoptic situation

Four days in the extended summer seasons of 2014 and 2015 representing typical organization types over Germany are selected for the case-studies conducted with ICON-LEM: 29 July 2014, 15 August 2014, 4 July 2015, and 5 July 2015. Three of the four cases (15 August 2014, 4 and 5 July 2015) were also analyzed by Brune *et al.* (2018) who investigated a complementary field-based approach for defining convective organization. Further details on the three cases are presented there. In the following, the synoptic conditions and principal organizational states are only briefly discussed.

On 29 July 2014 a small upper-level cut-off low moved from southern France in a southeasterly direction towards northern Italy and the surrounding Mediterranean region. Several weak low pressure systems meandering around Germany led to only weak large-scale forcing. Weak winds blew from a southeasterly direction. The southern part of Germany was under the influence of the upper-level low resulting in an overcast situation. In the middle and northern parts of the country, fair weather prevailed and convection developed in the morning and started to intensify around noon. Organization occurred in the afternoon resulting in a bigger convective system in northeastern Germany (Figure 1a). Overall, convective clusters were scattered across the country.

On 15 August 2014 an upper-level trough was stationary over Germany. The overall larger-scale forcing was weak. During the course of the day, two convergence lines crossed Germany. Overall light winds blew from a southwesterly direction. During the day a typical daily cycle of convection was observed with an increase in intensity and number of clusters from noon onwards. Clusters were scattered across the country and did not merge into multi-cell clusters (Figure 1b). The clusters also remained shallower than on 29 July 2014.

On the other hand, on 4 July 2015 Germany was under the influence of stronger larger-scale forcing. Deep convective clouds producing showers over the North Sea ahead of a warm front moved eastwards until 1400 UTC. From about 1400 UTC onwards, deep convective systems were mainly located over central and northern Germany. A clustering towards a larger system covering the northern part of the country occurred around 1900 UTC (Figure 1c). This cluster moved eastwards until midnight and ended covering large parts of eastern Germany. Overall, this day was characterized by highly organized explosive afternoon convection.

In the morning hours of the following day, 5 July 2015, deep convective large-sized clouds predominated over western Germany. In the afternoon, convection started mainly over the central and the northern part of the country triggered by a convergence line (Figure 1l) ahead of a cold front. At around 1800 UTC, a second line of convection directly coming along the approaching cold front merged with the first line of convection. This day was characterized by highly organized line-like convection.

2.3 | ICON-LEM

The ICON model includes three basic physics packages dedicated to numerical weather prediction, climate modelling and LES, respectively. In ICON the prognostic variables are solved on an unstructured triangular grid which is based on successive refinements of a spherical icosahedron (Wan *et al.*, 2013; Zängl *et al.*, 2015). ICON-LEM was shown to successfully represent dry convective and cumulus-topped boundary layers in the idealized set-up of doubly periodic boundary conditions and flat surfaces (Dipankar *et al.*, 2015).

Subgrid-scale turbulence is parametrized based on the diagnostic Smagorinsky scheme, including the modifications by Lilly (1962) to account for thermal stratification. The two-moment mixed-phase bulk microphysical parametrization of Seifert and Beheng (2006) is applied. Cloud fraction is diagnosed with a simple all-or-nothing scheme which does not account for fractional cloud cover at subgrid scales. The surface transfer scheme is based on Louis (1979). The multi-layer land-surface scheme Terra (Heise *et al.*, 2006) is used. Radiation is parametrized via the Rapid Radiation Transfer Model (Mlawer *et al.*, 1997).
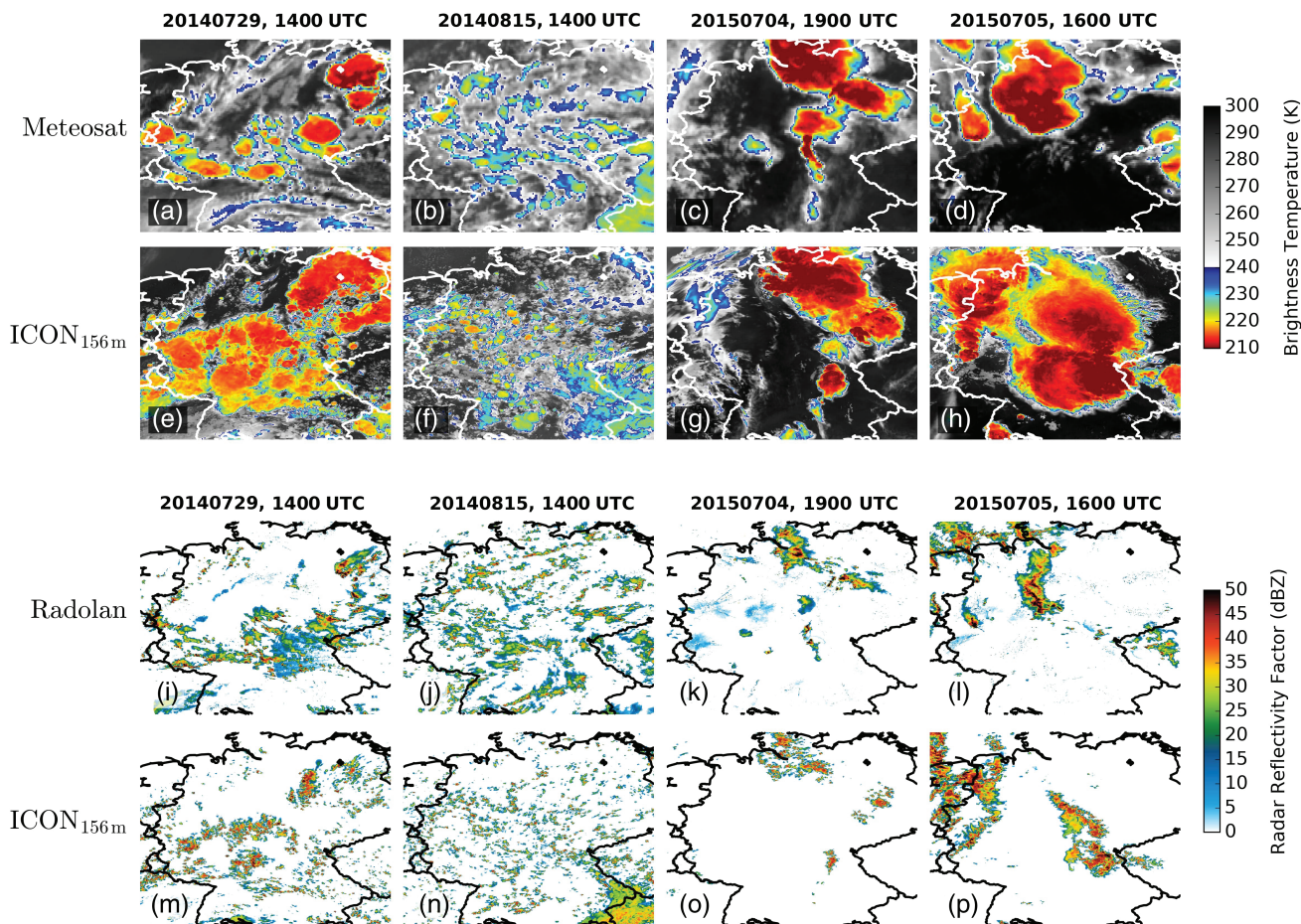
FIGURE 1 Overview of the spatial distribution of cloud tops and precipitation cores for four simulated days of deep convection over Germany. (a)–(d) Brightness temperature (BT) from Meteosat Second Generation, (e)–(h) synthetic BTs, (i)–(l) radar reflectivities from the Radolan RX product and (m)–(p) synthetic radar reflectivities. The synthetic datasets are generated by means of forward operators using ICON-LEM simulation outputs with grid spacing of 156 m

The ICON-LEM simulations performed for the four selected days used a limited-area set-up covering Germany (Figure 2). Lateral boundary conditions are taken from the COSMO model of the DWD (COSMO-DE). A multi-nesting approach is used to perform high-resolution simulations over Germany. In each refinement step, the grid spacing is halved from 625 m to 312 m and finally to 156 m in the innermost domain. Note that the square root of the mean triangle area is used as estimation for the grid spacing. A total of 150 vertical levels is used with grid stretching towards the model top at 21 km. The minimal layer thickness is 20 m near the surface and the lowest 1,000 m encompass 20 layers. A fast-physics time-step of 3 s is used for the coarsest resolution which is halved with each refinement. The simulation initialized at 0000 UTC from the operational COSMO-DE (Baldauf *et al.*, 2011) analysis covers 24 hr. The reason to initialize at midnight is that the model is already spun up by the time turbulence in the ICON model begins to develop during the morning and later when convection is usually strongest. The height-based terrain-following coordinate system used in the vertical is based on the smooth level vertical (SLEVE) coordinate implementation (Leuenberger *et al.*, 2010). At the lateral boundaries of the outer domain, the simulations are relaxed in a 20 km wide nudging zone towards COSMO-DE analysis at the synoptic times (0000, 0300, 0600, ..., 2100 UTC) and towards hourly COSMO-DE forecasts in between. A one-way nesting approach is chosen, which means that information is passed only from the coarser to the next finer grid. A complete description of the model configuration, the simulation set-up, and the model data is given in Heinze *et al.* (2017).

For this study we remap the output of the three nested ICON simulations onto a regular latitude–longitude grid with approximately 1.2 km spacing (the so-called *3d_coarse* outputs). These data are available from 0600 UTC onwards in 15 min output frequency for each simulated day. The overall analysis of observations and ICON simulations is limited to the intersection of the Radolan area and the area of the *3d_coarse* dataset (Figure 2). The simulations of 4 and 5 July 2015 were performed on a grid slightly shifted to the east given the overall synoptic evolution on that day (Figure 2).
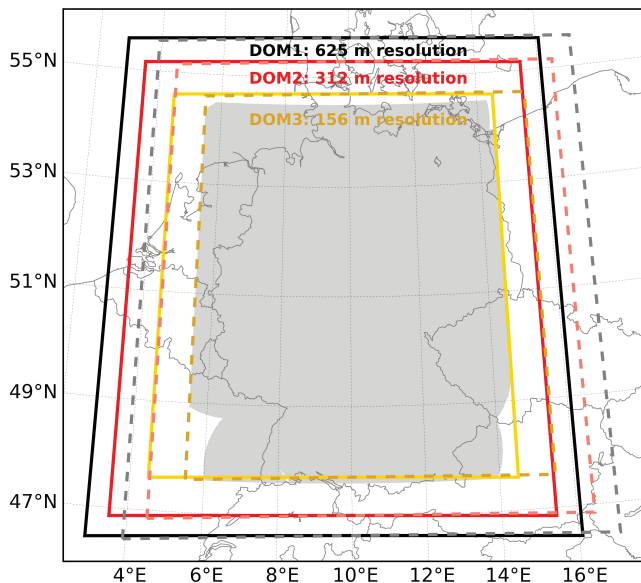
FIGURE 2 Area covered by the ICON-LEM simulations. The solid lines delineate the three model domains with grid spacings of 625, 312 and 156 m used for the simulations of 29 July 2014 and 15 August 2014. The dashed lines represent the domains slightly shifted towards the east used in the simulations of 4 and 5 July 2015. The filled innermost region, which represents the area covered by Radolan, is the domain used for analysis

2.4 | Model-derived data

The model prognostic variables are not directly comparable to the radar and satellite observations. For evaluating ICON in the observational space, synthetic radar reflectivities and synthetic satellite BTs have to be derived from the simulation outputs by means of forward operators (Blahak *et al.*, 2011).

We employ the non-polarimetric efficient modular volume radar operator (EMVORADO; Blahak, 2008; Blahak *et al.*, 2011; Zeng, 2013; Zeng *et al.*, 2016) to generate model-derived fields of radar reflectivity in offline mode. EMVORADO uses the two-moment bulk microphysical scheme (Seifert and Beheng, 2006) and requires the following model outputs for estimating radar reflectivity: temperature, pressure, rain mixing ratio, snow mixing ratio, specific graupel content, specific hail content, specific cloud ice content, specific cloud water content, specific humidity, number concentration cloud droplets, number concentration rain droplets, number concentration cloud ice, number concentration snow and geometric height at half level centre. The Mie-scattering theory is applied to compute the backscattering cross-sections of the hydrometeors and the use of look-up tables reduces the computing time (Jerger, 2014). The reflectivity is computed based on all types of hydrometeors. Raindrops are simulated as water spheres, cloud ice and graupel as one-layer spheres of a mixture of ice/air or ice/water/air for partially melted particles and snowflakes are simulated as two-layer spheres with a denser core and less denser shell. The

melting of ice categories is parametrized in EMVORADO (Bick, 2016).

For the generation of synthetic BTs, we apply a satellite forward operator to the thermodynamic and hydrometeor content profiles from the ICON simulation output. The forward operator sequentially performs single-column radiative transfer calculations with the RTTOV model version 11 (Saunders *et al.*, 1999) adapted to the spectral characteristics of MSG SEVIRI. Clear-sky radiances are calculated based on profiles of air pressure, temperature and humidity as well as several surface properties. For the computation of cloud-affected radiances, scattering and absorption properties of cloud particles are estimated from the hydrometeor mixing ratios. The configuration used has been applied operationally at the DWD for several years. For frozen hydrometeors, cloud ice and precipitating snow masses are simply added, and then the McFarquhar *et al.* (2003) scheme is applied to estimate the effective crystal sizes. This approach is similar to the SynSat method applied in earlier studies (e.g. in Keil *et al.*, 2006; Senf *et al.*, 2018) and the resulting model-derived BTs are ideally suited for a direct comparison with real satellite observations. The derived synthetic BTs typically have uncertainties in the order of several kelvins due to uncertainties in the specification of radiative properties of cloud particles (e.g. Senf and Deneke 2017 provide further discussion).

We apply the forward operators to the *3d_coarse* outputs and generate the synthetic reflectivities and BTs at 30 min intervals (0600, 0630, 0700, 0730, ..., 2330 UTC).

3 | METHODOLOGY

The threshold-based segmentation algorithm used to identify precipitation cores in the observed and model-derived reflectivities as well as cloud tops in the observed and model-derived BTs on the 1.2 km grid is described in Section 3.1. Section 3.2 presents a series of organization indices used to characterize the organizational state of convection.

3.1 | Segmentation algorithm

The method is similar to a watershed algorithm widely used in image processing and treats the BT field as a topographic map considering the local minima as basins in the relief. These basins are filled up with water from below until a certain water level is reached. In regions where different sources meet, dams are built to keep these regions separate. Furthermore, we apply a split-and-merge algorithm that splits up filament connections within one object and merges objects that share a large interface. More details are provided in Senf *et al.* (2018), including a list of parameters also chosen for the current study. For the reflectivity fields, the approach is slightly modified. Since precipitation cores are associated with higher values of
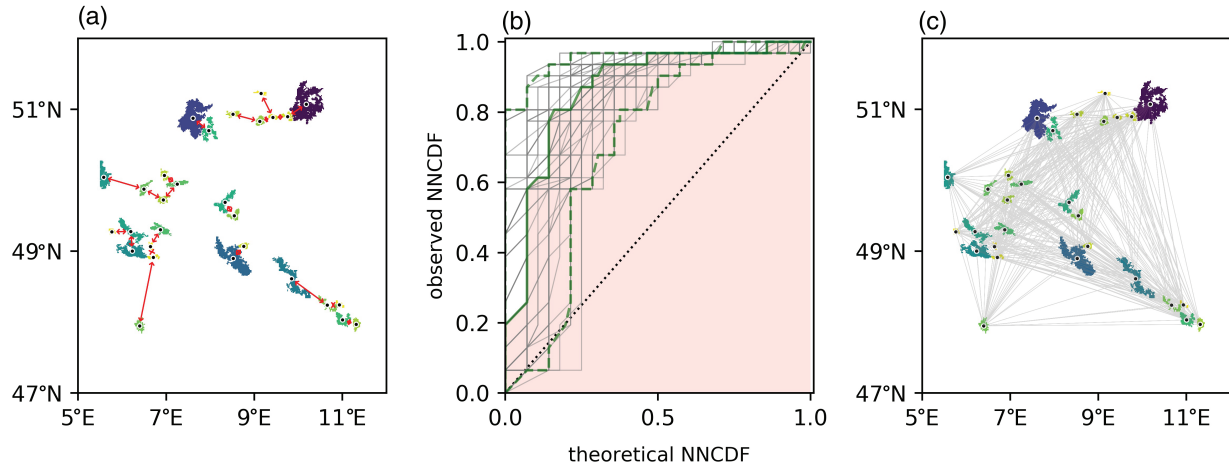
FIGURE 3 Schematic representation of (a) the nearest-neighbour connectivity approach of I_{org}, where only the distance to the nearest-neighbour object is considered (arrows) and (b) the corresponding observed versus theoretical NNCDFs from 100 different trials (curves). I_{org} indices are obtained by computing the area below each curve. The filled area below the single curve illustrates I_{org} median. The areas (not shown) below the dashed curves are the 2.5th and 97.5th I_{org} percentiles and are used to distinguish between the organizational states: organized, regularly distributed and randomly distributed. (c) The all-neighbours connectivity approach of SCAI and COP, for which the Euclidean distances between the centroid positions of all possible pairs of objects (lines) are considered. The geometric mean of these distances provide D_0

reflectivity, the method considers the local maxima instead of local minima. The local maxima are considered to be mountains in the relief and are filled up with water from above until a certain level is reached. As for BT, dams are built to keep different regions separate and the split-and-merge algorithm is applied as well. For the segmentation, only reflectivities ≥ 30 dBZ and BTs ≤ 240 K are considered. Moreover, only radar and satellite objects with a minimum size ≥ 30 and ≥ 40 grid cells are used, respectively. Note that the detection of radar objects is performed independently of the satellite object detection.

3.2 | Organization indices

Organized convection is hard to objectively define and may have different meanings depending on the application in mind. This has led to the definition of different organization indices in the past. Assuming a stochastic point process to describe the distribution of convective clouds, the spatial distribution of these points is important and can give information about the underlying physical mechanisms. Comparing nearest-neighbour (NN) distances against a reference distribution (e.g. from a Poisson process), one could on average assess if the organizational state of clouds tends to be either regularly distributed, randomly distributed or organized (e.g. Ramirez and Bras, 1990; Weger et al., 1992; Nair et al., 1998). Moreover, as the organization of convective cloud elements can lead to larger-size clumps, it might be beneficial to incorporate the sizes or shapes of the individual clouds in a convective organization index (Ramirez and Bras, 1990; White et al., 2018). If the same cloud coverage is distributed over different possible cloud clump configurations in a limited domain, then the cloud number decreases for

increasing clump sizes. Hence, also the cloud number could give information about organizational states. In the following description of organization indices, NN distances, object sizes and numbers will appear as integral parts of the respective definitions.

3.2.1 | Nearest-neighbour connectivity index

The organization index I_{org} has been recently applied to large-eddy simulations to assess the characteristics of trade-wind cumuli (Seifert and Heus, 2013) and to convection-permitting simulations to analyze the role of entrainment for organization of tropical deep convection (Tompkins and Semie, 2017). I_{org} is based on the NN connectivity approach (Figure 3a) and is able to classify the organizational states into organized, regularly distributed or randomly distributed. The objects are treated as discs (similar to Nair et al., 1998) and we use the edge-to-edge distance

$$d_{edge}(i, j) = d(i, j) - r_{equ}(i) - r_{equ}(j)$$

of these discs as an extension of the NN distance concept, where $d(i, j)$ is the distance between object centroid positions and $r_{equ}(i) = \sqrt{A(i)/\pi}$ is the equivalent radius of the ith object with area $A(i)$. In order to differentiate organization or regular distribution from randomness, the cumulative distribution function of the NN edge-to-edge distances (NNCDF) is compared to the NNCDF of theoretical objects randomly distributed in the same domain (Figure 3b). The unknown theoretical NNCDF can be estimated by applying a spatial Poisson process approach (Seifert and Heus, 2013; Tompkins

and Semie, 2017). However, here we follow the methodology of Weger *et al.* (1992) and Nair *et al.* (1998) which takes into account the size of the objects and approximates the theoretical NNCDF by randomly distributing discs with the size distribution of the observed objects in the domain. If the observed objects have NN edge-to-edge distances similar to the randomly distributed discs, the organizational state of the observations is random as well. If the observed NN distances are smaller than the randomly distributed objects, the observations are organized, while if the NN distances are greater, the observations are regularly distributed. Through the comparison of the observed NNCDF with the theoretical NNCDF, I_{org} is computed as the area below the curve in the comparison graph (the filled area in Figure 3b illustrates the computation of one I_{org}). A curve above the diagonal corresponds to I_{org} greater than 0.5 and implies organization, while a curve below the diagonal corresponds to I_{org} smaller than 0.5 and indicates regular distribution. A curve on the diagonal leads to I_{org} equal to 0.5 and the objects are randomly distributed. Especially for a small number of objects, a random distribution of discs may, however, be misinterpreted as organization or regular distribution. To differentiate organization from randomness with more accuracy, we proceed as follows:

(a) estimate the theoretical NNCDF 100 times and compute 100 different I_{org} indices;

(b) classify the organizational state as organized if the 2.5th I_{org} percentile (area below the lower dashed curve in Figure 3b) is greater than 0.5, regularly distributed if the 97.5th I_{org} percentile (area below the upper dashed curve in Figure 3b) is lower than 0.5; otherwise the scene cannot be differentiated from randomness.

3.2.2 | All-neighbours connectivity indices

Another organization index first proposed by Tobin *et al.* (2012) is the simple convective aggregation index (SCAI), which compares the number of objects in the domain (N) and the geometric mean distance (D_0) between the centroid positions of all possible pairs of objects (Figure 3c) to the possible maximum number of objects that can exist in the domain (N_{max}) and the characteristic domain size (L). This index reads

$$SCAI = \frac{N D_0}{N_{max} L} 1000. \qquad (1)$$

SCAI is therefore also interpreted as "the ratio of the degree of convective disaggregation to a potential maximal disaggregation" (Tobin *et al.*, 2012). We consider N_{max} equal to the number of grid cells of the analysis domain (filled innermost region in Figure 2) and use the southwest–northeast distance for L. In principle, the more organized, the lower the SCAI. However, this index has some limitations, since it is not scale-invariant, it is insensitive to

the size of the objects (White *et al.*, 2018) and it is not able to distinguish between organized, random and regular organizational states. Furthermore, it has been shown that SCAI is mainly dominated by the variability in N (Rempel *et al.*, 2017) which can lead to misinterpretations (Pearson *et al.*, 2014; Rempel *et al.*, 2017; Senf *et al.*, 2018; White *et al.*, 2018).

In order to overcome some deficiencies of SCAI, White *et al.* (2018) proposed the convective organization potential (COP) index based on the hypothetical interaction potential between objects

$$V(i,j) = \frac{\sqrt{A(i)} + \sqrt{A(j)}}{d(i,j)\sqrt{\pi}},$$

and defined as

$$COP = \frac{\sum_{i=1}^{N} \sum_{j=i+1}^{N} V(i,j)}{\frac{1}{2} N(N-1)}. \qquad (2)$$

Larger objects located closer to each other increase COP (White *et al.*, 2018 give more detail).

Since COP as well as I_{org} and SCAI are not defined for a single object, only scenarios with at least two objects are considered in this study.

3.2.3 | 2D shape index

In addition to the organizational state, we also quantify the dominant 2D shape of the objects. Shape indices have long been used in other research areas as for computer form identification (Duda and Hart, 1973) and urban morphology (Lo, 1980). Maceachren (1985) and Xia (1996) use a perimeter-area measurement to investigate geographic shapes. We propose to apply this measure to identify the 2D shape of radar and satellite objects. The index I_{shape} is defined as

$$I_{shape} = \frac{1}{N} \sum_{i=1}^{N} s(i), \qquad (3)$$

with the shape ratio $s(i)$ for each object computed as

$$s(i) = \frac{P_{eq}(i)}{P(i)}, \qquad (4)$$

where $P(i)$ is the actual perimeter of the object i and $P_{eq}(i) = \sqrt{4\pi A(i)}$ is the perimeter of an equivalent area-equal disc. The perimeter $P(i)$ is computed as the contour line through the centres of the border grid cells of the objects (van der Walt *et al.*, 2014; Benkrid and Crookes, 2000), where the grid cells are considered to be squared. Objects with $s(i)$ between 0.5 and 1.0 are more compact than objects for which the ratio is between 0.0 and 0.5. I_{shape} is the mean of $s(i)$

computed over the total number of objects and provides the average shape in the domain. An I_{shape} close to one indicates that the most representative shape in the domain is a disc, whereas for I_{shape} close to zero a line is the most representative shape.

4 | RESULTS

In the following, Section 4.1 discusses the organizational state of observed cloud tops and precipitation cores for the extended summer seasons of the years 2014 and 2015. Section 4.2 examines potential relationships between the organizational state and the objects characteristics and Section 4.3 discusses changes in organization throughout the diurnal cycle. Finally, in Section 4.4 the simulations are evaluated against the radar and satellite observations for the four selected days in terms of their ability to represent organization.

4.1 | How organized is convection over Germany?

In order to determine the organizational state of convection over Germany, we start our analysis by investigating the time series of the organization indices based on Radolan and Meteosat observations.

Precipitation cores and cloud tops present a tendency towards organization as revealed in the time series of I_{org} (Figures 4a and 5a). Considering both years and based on the I_{org} confidence interval (Section 3.2), precipitation cores are organized, regularly distributed and randomly distributed for 92.1, 0.4 and 7.5% of the time, respectively. For cloud tops, the frequency of each organizational state is different, i.e. organization, regular distribution and random distribution occur for 69.3, 0.6 and 30.1% of the time, respectively. The lower frequency of organized and the higher frequency of randomly distributed cloud tops is partly due to the smaller number of Meteosat objects and their larger areas (Figures 4f, 5f, 4c and 5c). In situations with only a few large objects, a broader I_{org} distribution is obtained and hence, even for rather organized objects, an organizational state significantly different from randomness can not be identified. The organizational state of precipitation cores is difficult to assess from cloud-top observations, and *vice versa* (Figures 4i and 5i), as suggested by the low correlation between the Radolan and Meteosat median I_{org} of +0.15 in 2014 (Figure 4i) and +0.17 in 2015 (Figure 5i) and reinforced by the low correlation of +0.05 in 2014 and +0.003 in 2015 between Radolan and Meteosat 2.5th I_{org} percentile and the correlation of +0.19 in 2014 and +0.17 in 2015 between the corresponding 97.5th I_{org} percentile.

Cloud tops present greater interaction potential (larger COP values) than precipitation cores (Figures 4b and 5b),

which is mostly attributed to the larger cloud-top areas (Figures 4c and 5c), since on average the distances between the cloud-top centroids are similar to the distances between the precipitation core centroids (Figures 4d and 5d). Although significant, there are low correlations for COP, D_0 and object areas between Radolan and Meteosat (Figures 4j-l and 5j–l).

The strong dependence of SCAI on N (compare Figures 4e and 4f, and Figures 5e and 5f) as found in previous studies (Rempel *et al.*, 2017; White *et al.*, 2018) is reinforced by our investigation. Due to the fact that numerous precipitation cores can be embedded in clouds with large coverage, SCAI is larger for Radolan than for Meteosat objects. Between Radolan and Meteosat there is a correlation of +0.58 and +0.54 for $SCAI$ and N in 2014, respectively (Figures 4m–n). This shows evidence that, although the number of Radolan and Meteosat objects is different, the increase in cloud-top number is associated with an increase in precipitation cores. However, this relationship is weaker in 2015 with a corresponding correlation of +0.36 and +0.34 for SCAI and N, respectively (Figures 5m–n).

The dominant 2D shape of the objects varies between elliptical and circular (Figures 4g and 5g), however with very low correlation between precipitation cores and cloud tops (Figures 4o and 5o).

The impact of the organizational state on rainfall is assessed through the correlation between the total rainfall (Figures 4h and 5h) and the organization indices. The total rainfall is computed as the area integral of the rainfall rates (RY-product) over the object areas and is hereinafter referred to as rainfall. No significant correlation with median I_{org}, COP and I_{shape} is found, however we observe positive correlations between rainfall and SCAI (+0.69), N (+0.72) and object areas (+0.52). Similar results have been shown by Tobin *et al.* (2012), who found correlation between the number of objects identified in satellite BT data and the precipitable water.

From this first investigation, observations from two instruments (e.g. radar, satellite) reveal weak association in the organizational state between precipitation cores and cloud tops. Furthermore, although convection is more frequently organized than randomly or regularly distributed over Germany, organization does not seem to impact rainfall. Instead, rainfall increases with the increase in N and in object areas independent of the organizational state. Motivated by these results, we investigate whether there are typical differences between organization, random distribution and regular distribution. To this end, we scrutinize in the next section the relationship between the I_{org}-based organizational states and the object characteristics, including the amount of rainfall. Furthermore, we investigate whether the organization indices I_{org}, SCAI and COP are able to consistently identify organization.
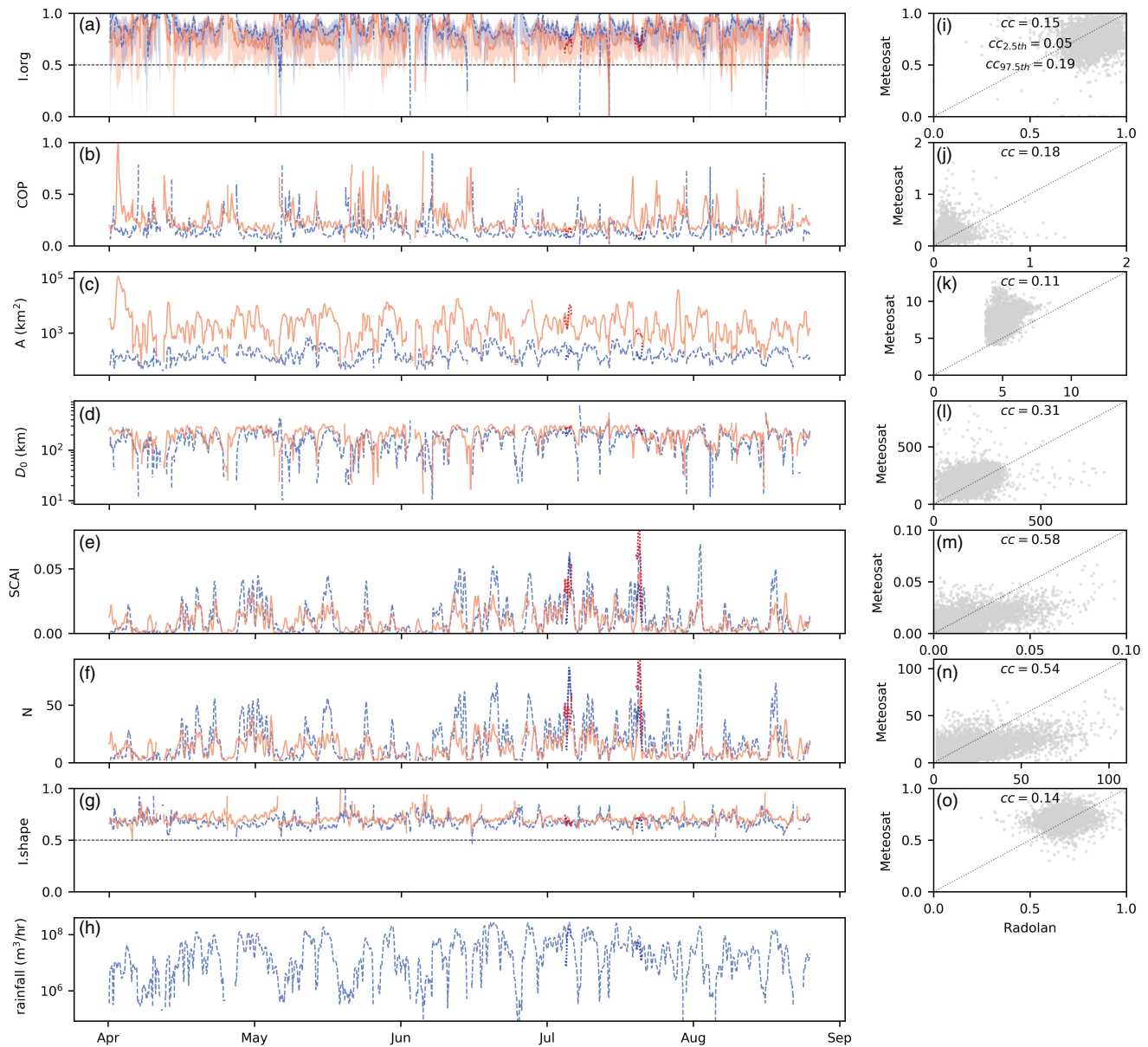
FIGURE 4 (a) Median I_{org}, (b) COP, (c) object areas, (d) D_0, (e) SCAI, (f) N, (g) I_{shape} and (h) rainfall produced by the objects between 1 April 2014 0000 UTC and 30 September 2014 2330 UTC. The shaded areas in (a) represent the 2.5th and 97.5th confidence interval of I_{org} estimated from 100 different trials. The indices based on Radolan are represented in dashed lines, and full lines represent the indices computed for Meteosat. Rainfall is computed as the area integral of the Radolan rainfall rates (RY-product) over the object areas in the domain. The object area in (c) is the area of all objects in the domain averaged over N. The dotted lines in (a)–(h) represent the indices for 29 July 2014 and 15 August 2014 computed from the model-derived BT and reflectivities with 625 m grid spacing. All indices are computed with a time step of 30 min. For visualization purposes, the time series were filtered using a moving mean filter with window equal 23 (23 time steps of 30 min). (i)–(o) show the scatter plots and the correlation coefficients of the indices in (a)–(g) between Meteosat and Radolan. In (i) $cc_{2.5th}$ indicates the correlation between Radolan and Meteosat 2.5 I_{org} percentile, whereas $cc_{97.5th}$ shows the correlation between Radolan and Meteosat 97.5th I_{org} percentile. Correlation is computed using the original 30 min indices

4.2 | Relationship between the organizational states and the object characteristics

In order to better characterize typical organized from non-organized states, we first address in this section the question whether differences in (a) the object characteristics

and (b) rainfall can be identified between organization, regular distribution and random distribution. To this end, we classify the object areas, N and rainfall for the extended summer period of both years 2014 and 2015 into the three I_{org}-based organizational states and calculate the conditional mean for each quantity (Figures 6a–c). We compare the means of the object areas, N and rainfall between organization and
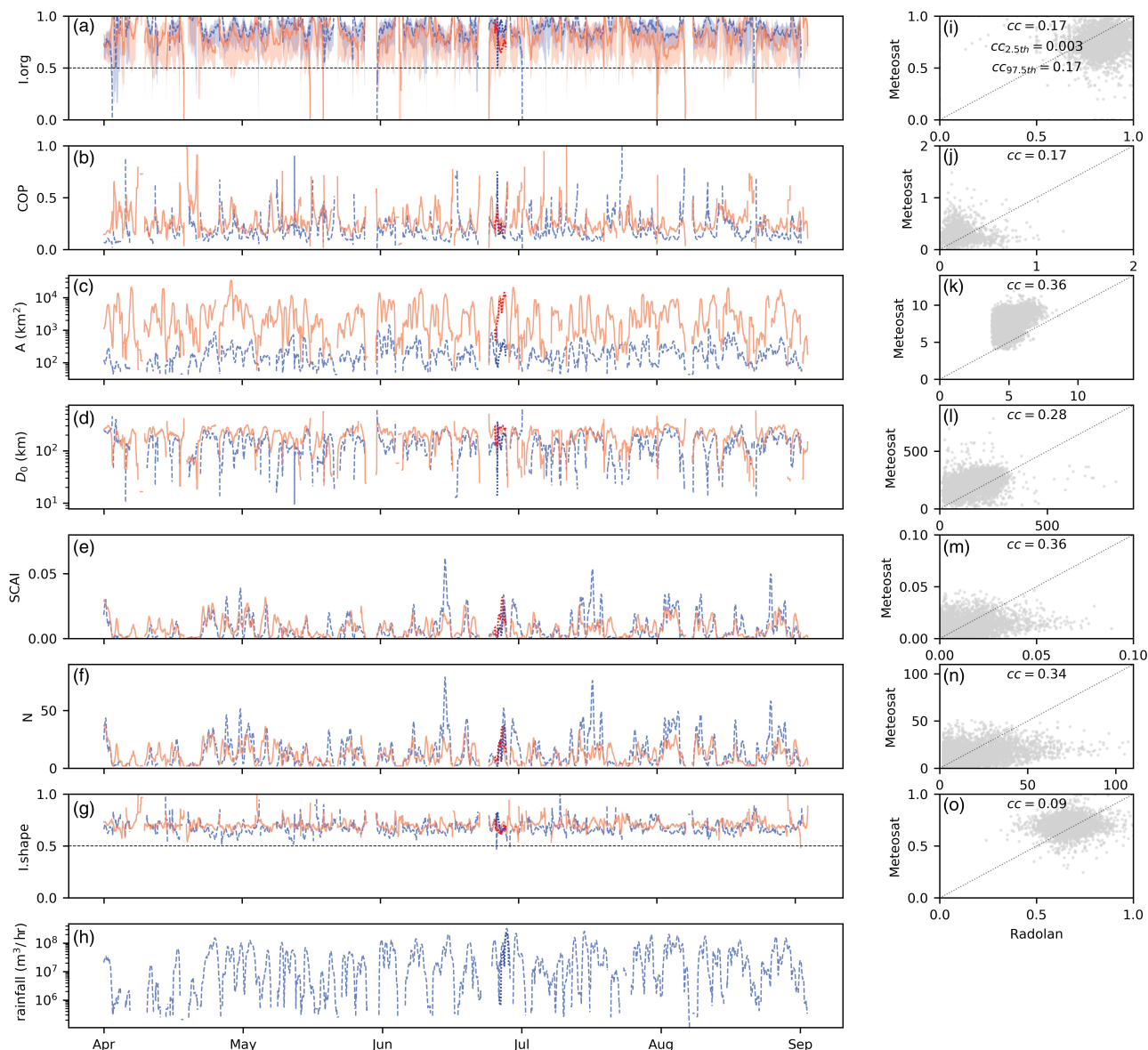
FIGURE 5 As Figure 4, but for the time period between 1 April 2015 0000 UTC and 30 September 2015 2330 UTC. The dotted lines in (a)–(h) represent the indices for 4–5 July 2015

random distribution, organization and regular distribution and between random and regular distribution (Figures 6a–c). For testing the null hypothesis of equal means in those comparisons, we perform the two sample *t*-test for equal means (Snedecor and Cochran, 1989) at the 0.05 significance level. The statistical test is performed for Radolan and Meteosat separately. The scenarios for which the null hypothesis is rejected are described in the following. The precipitation cores are larger for organization than for the random distribution (Figure 6a), while rainfall and *N* are also the largest in organization (Figures 6b–c). For cloud tops there are differences in their areas, *N* and rainfall among all three organizational states (Figures 6a–c). In contrast to precipitation cores, the largest cloud tops and rainfall are found for the random distribution (Figures 6a and 6c). However, in agreement with precipitation cores, the largest number of cloud

tops occurs in organization as well (Figure 6b). The reliability of the results for cloud tops may be critical, as mentioned in Section 4.1, since the spatial distribution of fewer larger objects is harder to significantly discriminate from random distribution. Among the three organizational states, the regular distribution shows the lowest *N* in both Radolan and Meteosat (Figure 6b), with the lowest rainfall (Figure 6c) and small object areas (Figure 6a). In summary, large *N* is a clear characteristic of organization, whereas small *N* features regular distribution. Large object areas are characteristics of both organization and random distribution, and rainfall again shows to be a reflection of either *N* or object area.

The lack of relationship between rainfall and the organizational states of convection is reinforced by the analysis of rainfall intensity (Figure 6d). For this investigation, we compute the rainfall intensity of Radolan and Meteosat objects
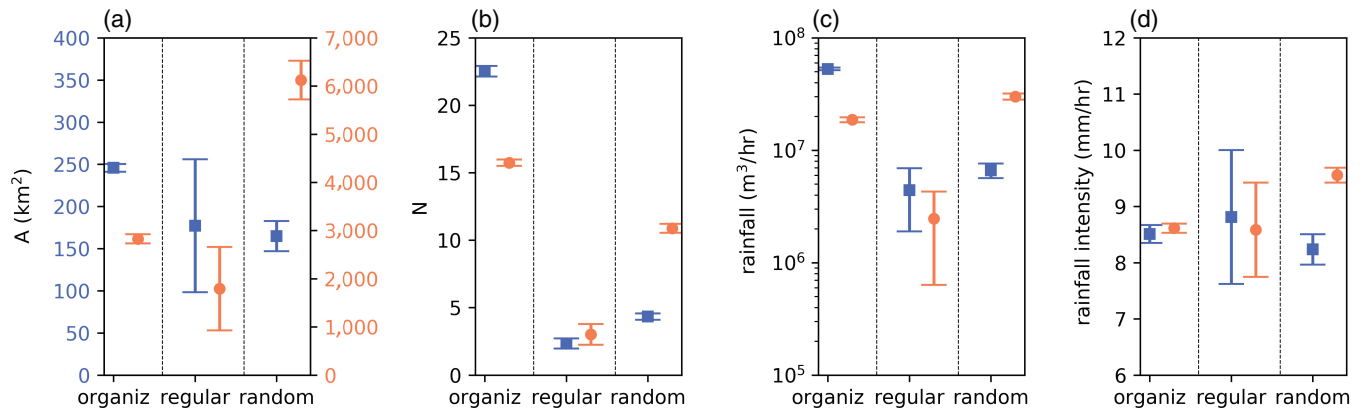
FIGURE 6 Conditional mean value and error of the mean of the (a) object areas, (b) N, (c) rainfall and (d) rainfall intensity produced by the Radolan (square) and Meteosat (circle) objects for organization, regular distribution and random distribution. The rainfall intensity is the sum of the rainfall rate of the object grid cells averaged over the total number of object grid cells in the domain. For the computation of rainfall intensity mean value, only scenarios with number of precipitation cores satisfying $2 \leq N \leq 8$ and areas between 40 and $1,500\,\mathrm{km}^2$ are considered. For cloud tops, the included scenarios satisfy $2 \leq N \leq 17$ with areas between 60 and $16,000\,\mathrm{km}^2$

(independently) at each time step (30 min). The rainfall intensity is computed as the sum of the objects grid cells rainfall rate (Radolan RY-product) averaged over the total number of objects grid cells in the domain. In order to limit the impact of the objects area and of N on the rainfall intensity, we consider here only scenarios with similar N and similar object areas throughout the different organizational states. Since the regular distribution shows the smallest N and object areas, we limit the organized and randomly distributed scenarios also to similar N and similar areas. Hence, scenarios with number of precipitation cores that satisfy $2 \leq \mathrm{N} \leq 8$ with areas between 40 and $1,500\,km^2$ are considered. For cloud tops, the scenarios need to satisfy $2 \leq \mathrm{N} \leq 17$ and the object areas need to be between 60 and $16,000\,km^2$. Rainfall intensity of these scenarios is classified as function of the three organizational states, the conditional means are computed and the two sample t-test for equal means is performed. Precipitation cores do not exhibit statistically significant difference between means among the three organizational states (Figure 6d), suggesting that on average the intensity of rainfall produced by the clouds in similar scenarios (N, area) is not influenced by the organizational state. Note that, although Meteosat shows stronger rainfall intensity for the random distribution than for organization, this result may be more critical since rainfall intensity is estimated from radar data.

In a second step, we investigate whether there is a relationship among the different organization indices including their connections to rainfall and to object areas (Figure 7) and whether they are able to characterize organization consistently. COP identifies higher degree of organization for I_{org}-based organization than for I_{org}-based random and regular distribution (Figure 7a), that is, COP increases with I_{org}. For SCAI, the situation is different as the index exhibits a non-monotonic behaviour (Figure 7b) increasing up to a maximum, where median I_{org} is around 0.75 for Radolan and 0.65 for Meteosat and decreasing again for larger I_{org} values. For median I_{org} lower than 0.5 (regular distribution) and median I_{org} greater than 0.8 (organization), SCAI indicates increase in the degree of organization. However, for I_{org}-based organization with median I_{org} between 0.5 and 0.8, for which COP also indicates an increase in the organization's degree (Figures 7a–b), SCAI suggests less organization. The latter results from the fact that N increases in those scenarios (not shown) and hence SCAI increases. Given that SCAI approaches organization focusing on N and the distances between the object centroids, while I.org and COP consider also the size of the objects, some scenarios may be best characterized by the combined use of the three organization indices. We discuss this further in Section 4.4.3, where we evaluate the model simulations by means of the organization indices. The analysis of rainfall in combination with SCAI and the object areas as functions of I_{org} (Figures 7b–d) is in agreement with the results of Tobin *et al.* (2012) and our results of the first part: rainfall is impacted by N and by the object areas. Rainfall of Radolan objects increases as N and object areas increase (rainfall in Figure 7c, SCAI in Figure 7b and object areas in Figure 7d for median I_{org} between 0.5 and 0.8). In contrast to Radolan, Meteosat objects show this behaviour for the random distribution (rainfall in Figure 7c, SCAI in Figure 7b and object areas in Figure 7d for median I_{org} between 0.4 and 0.6).

In summary, these investigations are in agreement with Tobin *et al.* (2012) and reinforce our results of the first part, that is, Radolan objects show increase in rainfall for organization due to the increase in N and not due to increase in the rainfall intensity. In the next section we investigate whether the organizational state of precipitation cores and cloud tops exhibits a diurnal cycle.
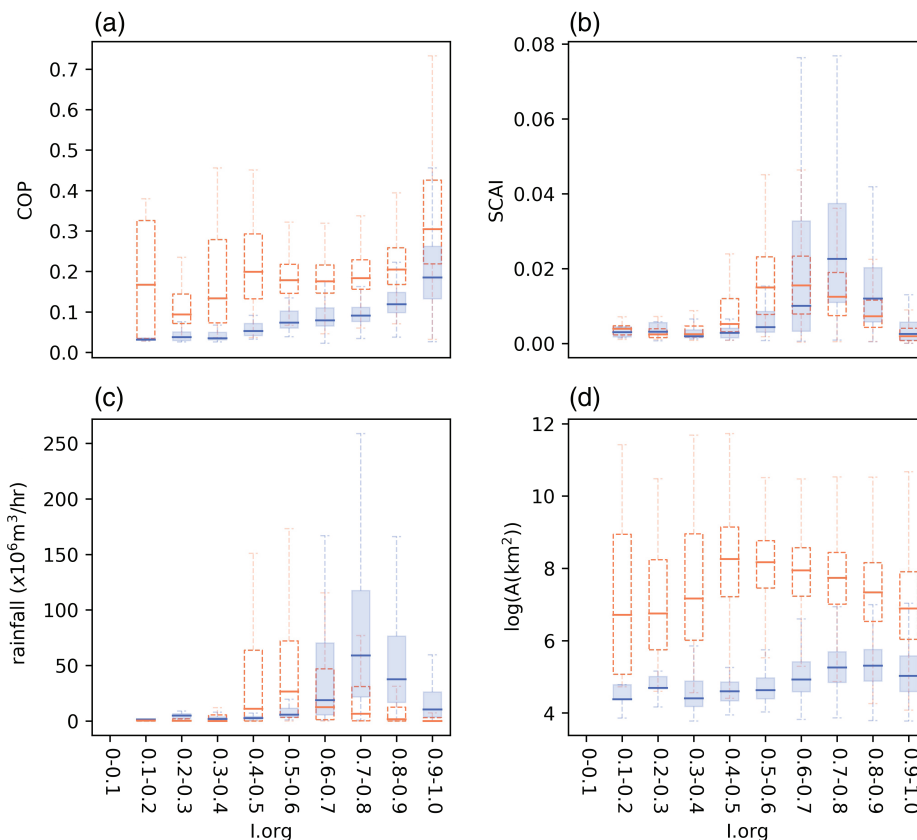
FIGURE 7 (a) COP, (b) SCAI, (c) rainfall produced by the objects and (d) object areas as function of median I_{org} for Radolan (filled) and Meteosat (unfilled). The bottom of the boxes indicates the 25th percentile, and the top indicates the 75th percentile. The line inside the boxes illustrates the median. The whiskers represent the range over which the data vary. For this computation the 30 min data from 1 April 0000 UTC to 30 September 2330 UTC of both years 2014 and 2015 are used

4.3 | Diurnal cycle of organization

For assessing the diurnal cycle of organization indices and of object characteristics, we make certain that the phase of the diurnal cycle is robust across the days selected for compositing. To this end, we only use the days for which the maximum rainfall occurs between 1500 and 1800 UTC and it is at least a factor 2 greater than the minimum rainfall on that day (Figure 8). I_{org} and COP do not exhibit significant diurnal cycle (Figures 8a–b) in the organizational state, which is reinforced by D_0 (Figure 8d) showing similar distance between object centroids on average in the course of the day. On the other hand, SCAI, N and rainfall show a clear diurnal cycle (Figures 8e–f and 8h) with noticeable increase in the number of objects and in rainfall after 1200 UTC. SCAI suggests decrease in the degree of organization which increases again after 1800 UTC. The cloud-top areas (Figure 8c) and the 2D shape of precipitation cores (Figure 8g) show a rather slight diurnal cycle, however, in agreement with rainfall, i.e. rainfall increases after 1200 UTC, when the objects are larger and tending towards a more circular shape.

To summarize, the diurnal cycle of rainfall is in agreement with the diurnal cycle of N. On the other hand, since SCAI is highly influenced by N, and I_{org} and COP do not

exhibit significant changes in the course of the day, we conclude that there is not enough evidence of a diurnal cycle in the organizational state of precipitation cores and of cloud tops.

In the next section, we evaluate the ability of synthetic reflectivities and BTs derived from the ICON-LEM simulation outputs to reproduce the Radolan and Meteosat observations. Moreover, we also evaluate the ability of the simulations to represent the sizes of the objects and their organizational states.

4.4 | Model evaluation

During the course of the HD(CP)² project, ICON-LEM has been further developed including solutions for problems detected while analyzing first simulated days. Bugs in cloud microphysics (wrong homogeneous freezing rate, missing call of saturation adjustment), a wrong OpenMP call in the turbulence scheme and the underestimation of the surface momentum flux by an order of magnitude have been detected after this study was performed. It has not been feasible to re-simulate all days entering this study. However, to estimate the combined impact of these bugs, 29 July 2014 has been
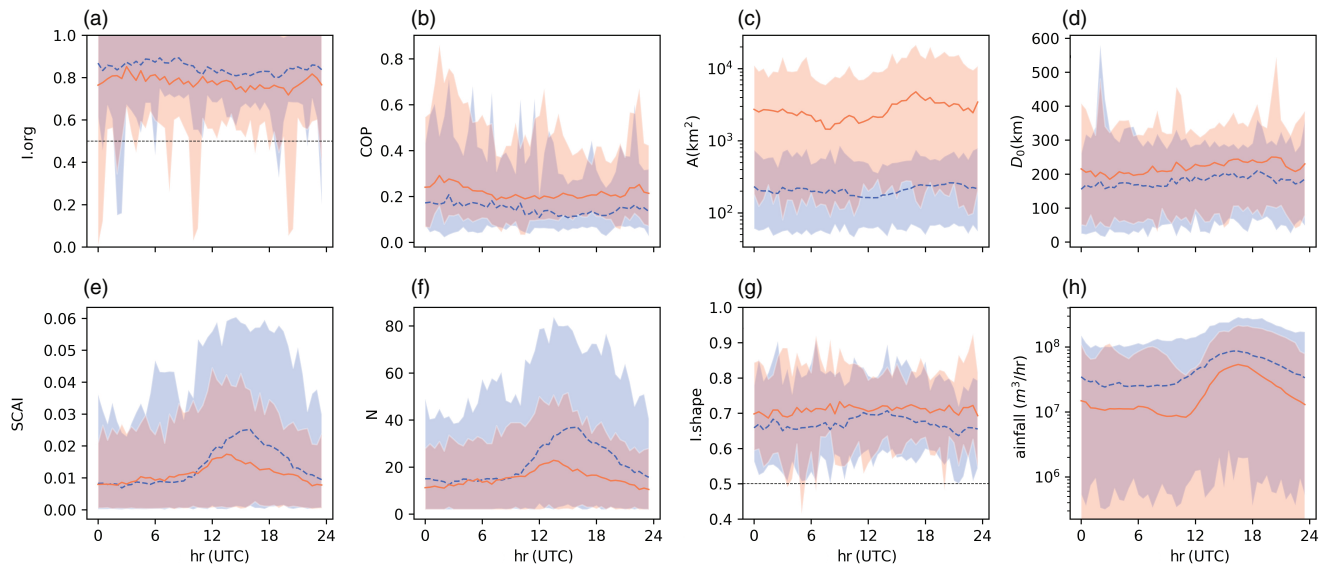
FIGURE 8 Diurnal cycle composite of (a) median I_{org}, (b) COP, (c) object areas, (d) D_0, (e) SCAI, (f) N, (g) I_{shape} and (h) rainfall. The lines represent the mean (dashed for Radolan and full for Meteosat) and the shaded areas represent the 2.5th–97.5th percentile interval of the quantities. The mean and the percentiles are computed based on 73 events (30 min) for Radolan and 55 events for Meteosat selected within the period from 1 April 0000 UTC to 30 September 2330 UTC of the years 2014 and 2015. The object area is the sum of all object areas in the domain divided by the number of objects. Rainfall is the area integral of the Radolan rainfall rates over the object areas in the domain

re-simulated with all the bugs fixed. The analysis (not shown) reveals only minor differences in the equivalent radius of the objects, in the rainfall rate and in the diurnal cycle of the organization indices obtained from the synthetic observations. Overall, we conclude that, despite using output from model runs with bugs in the code, the results we present here for the four selected days of convection are still reliable and insensitive to these bugs.

4.4.1 | Model-derived reflectivity and brightness temperature

Synthetic datasets are generated by applying EMVORADO and the satellite forward operator to the outputs of ICON simulations with grid spacings of 625, 312 and 156 m (Section 2.4). Histograms of model-derived reflectivities, BTs and simulated rainfall rates of the detected objects are compared with the histograms of their observational counterparts averaged over the selected days (Figure 9). The frequency of occurrence is significantly underestimated by the model in all three grid spacings for most of the reflectivity and rainfall rate intervals (Figures 9a and 9c), especially for rainfall rates lower than 16 mm/hr. The frequency of BTs between 212 and 240 K (Figure 9b) is overestimated at all three grid spacings, whereas BTs lower than 208 K, which are related to very deep convection, are underestimated in their occurrence. Decreasing the ICON grid spacing from 625 to 156 m does not seem to provide systematic improvements in the representation of rainfall rates and cloud-top BTs, hinting towards deficits in the applied mixed-phase and ice microphysics parametrization.

4.4.2 | Size of the objects

The size distribution of precipitation cores and cloud tops is reasonably well represented by the model-derived data (Figures 10a–b). The most frequent precipitation cores observed in Radolan (Figure 10a) with equivalent radii in the interval 3–5 km are overestimated in their occurrence by the model-derived data with 625 m and underestimated at finer grid spacings. On the other hand, the occurrence of objects with an equivalent radius greater than 5 km is underestimated at all grid spacings and no model-derived object is found in the maximum observed equivalent radius interval 70–90 km.

The most frequent Meteosat cloud tops with equivalent radii in the interval 10–20 km (Figure 10b) are overestimated in their occurrence. The best agreement between model-derived and Meteosat is found for objects in the equivalent radii intervals 20–30 and 70–100 km. The model overestimates the frequency of objects with equivalent radii greater than 100 km and, unlike Meteosat, simulates objects with maximum equivalent radii in the interval 300–400 km. As for the evaluation of reflectivity and BT, these results indicate no improvement in the representation of the object sizes by decreasing the grid spacing from 625 to 156 m.

4.4.3 | Organization indices

For assessing the performance of ICON-LEM to represent the organizational states of convection, we compute the organization indices for the simulations and compare them with the indices computed for the observations. The model is able to reproduce similar organization indices, object areas,
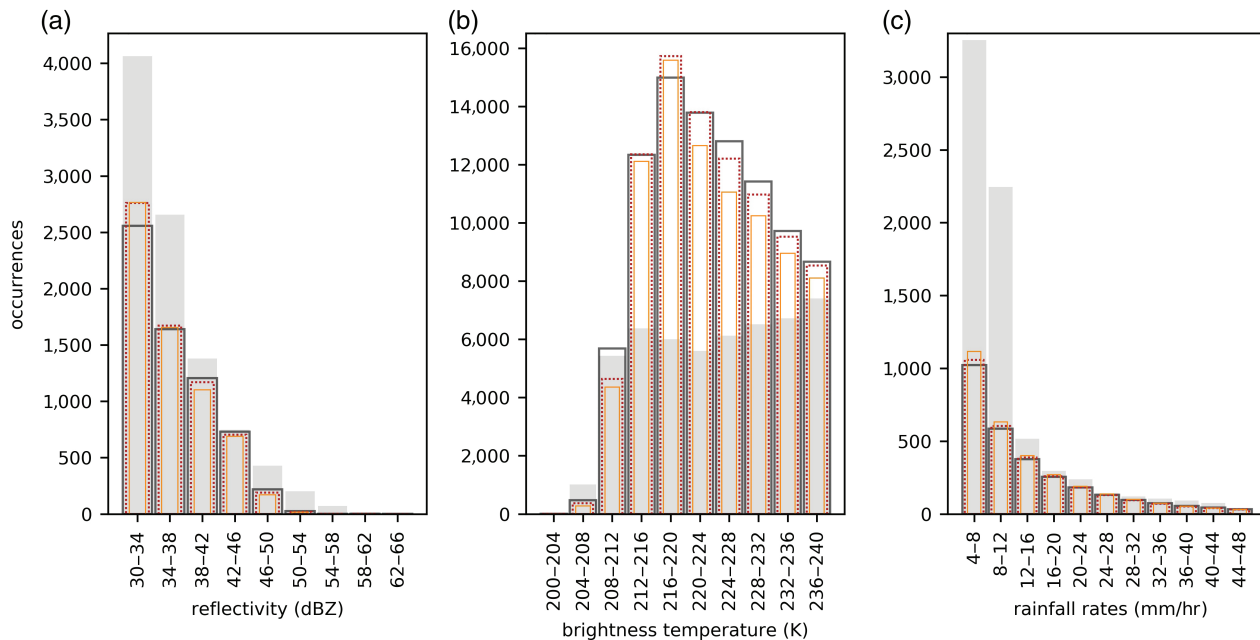
FIGURE 9 (a) Reflectivity, (b) BT and (c) rainfall rates. Observations are represented by the filled bars, unfilled bars show the model-derived data with 625 m (thick line), 312 m (dotted line) and 156 m (thin line) grid spacings. The histograms are composites averaged over the convective cases of 29 July 2014, 15 August 2014, 4 and 5 July 2015
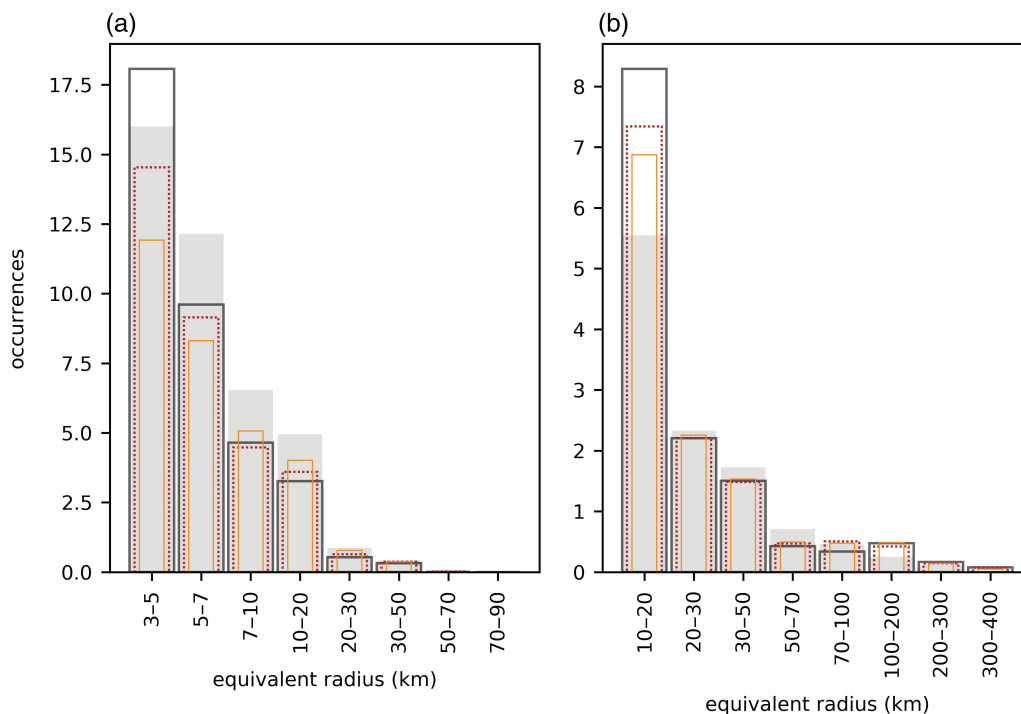

FIGURE 10 As Figure 9, but for equivalent radius of objects derived from (a) radar reflectivities and (b) satellite BTs

D_0, N, and rainfall to those observed in the extended summer of the years 2014 and 2015 (dotted lines in Figures 4a–h and 5a–h).

Precipitation cores are predominantly organized during the four selected days (Figures 11a–d). I_{org} is larger for 4 and 5 July 2015, when clusters are less scattered across Germany (Figures 1k–l), indicating higher degree of organization

than for the events in 2014. These behaviours are well represented in the simulations without significant differences among the three grid spacings (Figures 11a–d). For cloud tops, the observed organizational states vary between organization and random distribution (Figures 12a–d) and there is greater diurnal variability of I_{org} in 2015 than 2014. The model-derived I_{org} is not sensitive to the grid spacings
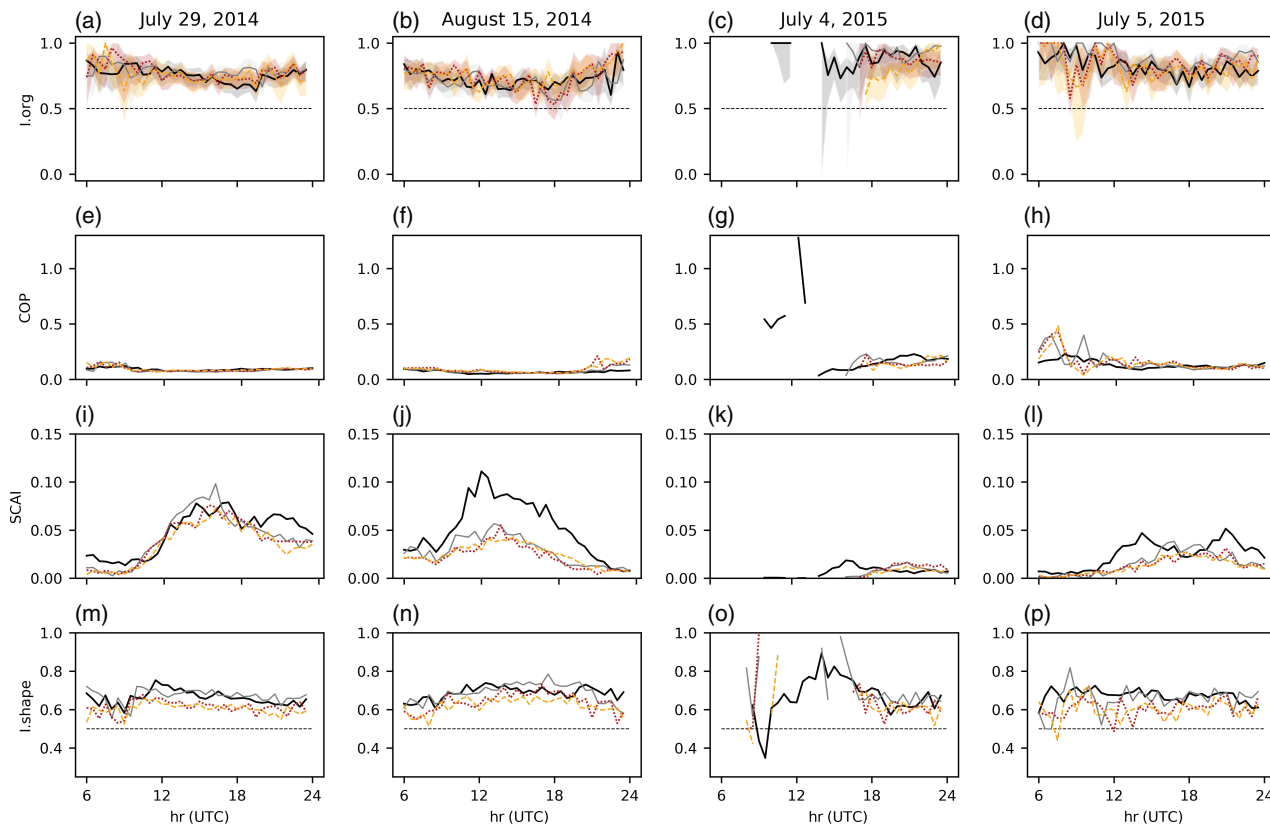
FIGURE 11 (a–d) Median I_{org}, (e–h) COP, (i–l) SCAI and (m–p) I_{shape} based on Radolan (thick line) and model-derived reflectivity from simulations with 625 m (thin line), 312 m (dotted line) and 156 m (dashed line) grid spacing for the four days 29 July 2014, 15 August 2014, 4 and 5 July 2015. The shaded areas in (a–d) represent the 2.5th–97.5th confidence interval of I_{org} estimated from 100 different trials. The missing data in (c), (g), (k) and (o) are due to scenarios with $N < 2$

either. However, in contrast to precipitation cores, the model shows lower performance in representing the diurnal cycle of cloud-top organizational states (Figures 12a–d).

COP and SCAI (Figures 11e–l and 12e–l) show also evidence for higher degree of organization in precipitation cores and cloud tops during the events in 2015 (larger COP and smaller SCAI) than 2014. On 4 and 5 July 2015 precipitation cores and cloud tops are larger (larger COP), however, in smaller numbers (lower SCAI) than on 29 July and 15 August 2014, when the clusters are more scattered across the country (Figures 1a–b and 1i–j). The more pronounced diurnal cycle of COP (and hence, of object areas) in 2015, especially for cloud tops, may explain the corresponding larger variability in I_{org} in 2015 than in 2014. The larger SCAI for the convective events in 2014, indicating larger N, is in agreement with the corresponding smaller I_{org}, especially for precipitation cores. Compared to observations, the model-derived COP is best reproduced for situations with less pronounced diurnal cycle, for example, COP for precipitation cores is better represented than for cloud tops, especially for the events in 2015 (Figures 11g–h and 12g–h). Regarding the number of objects, the model-derived SCAI suggests underestimation of the number of precipitation cores and overestimation of the number of cloud tops across all three grid spacings (cf.

Figures 11i–l and 12i–l). Notice that on 15 August 2014, the day with the smallest objects (Figure 1b) among the selected days, different grid spacings show significant differences in SCAI for cloud tops (Figure 12j) with improvement for the simulations with the finest grid spacing. However, for precipitation cores (Figure 11j), the simulations underestimate SCAI and there is no significant difference in the performance across grid spacings.

In addition to the organizational states, the 2D shapes show particular differences between the events in 2014 and 2015 as well (Figures 11m–p and 12m–p). For 4 and 5 July 2015, when the objects are larger and less numerous, the shapes vary between elliptical lines and more circular shapes (I_{shape} between 0.3 and 0.9), whereas for the cases in 2014, when there are more and smaller objects more scattered across the country, the shapes tend towards being more circular ($I_{shape} \approx 0.7$). Simulations with 625 m grid spacing show an improvement over the finest grid spacings, which produce precipitation cores and cloud tops with lower aspect ratios than observed. Based on the investigated cases, I_{shape} seems to be the index with the highest sensitivity to the model grid spacings, especially for modelling cloud-top shapes (Figures 12m–p). The coarsest considered
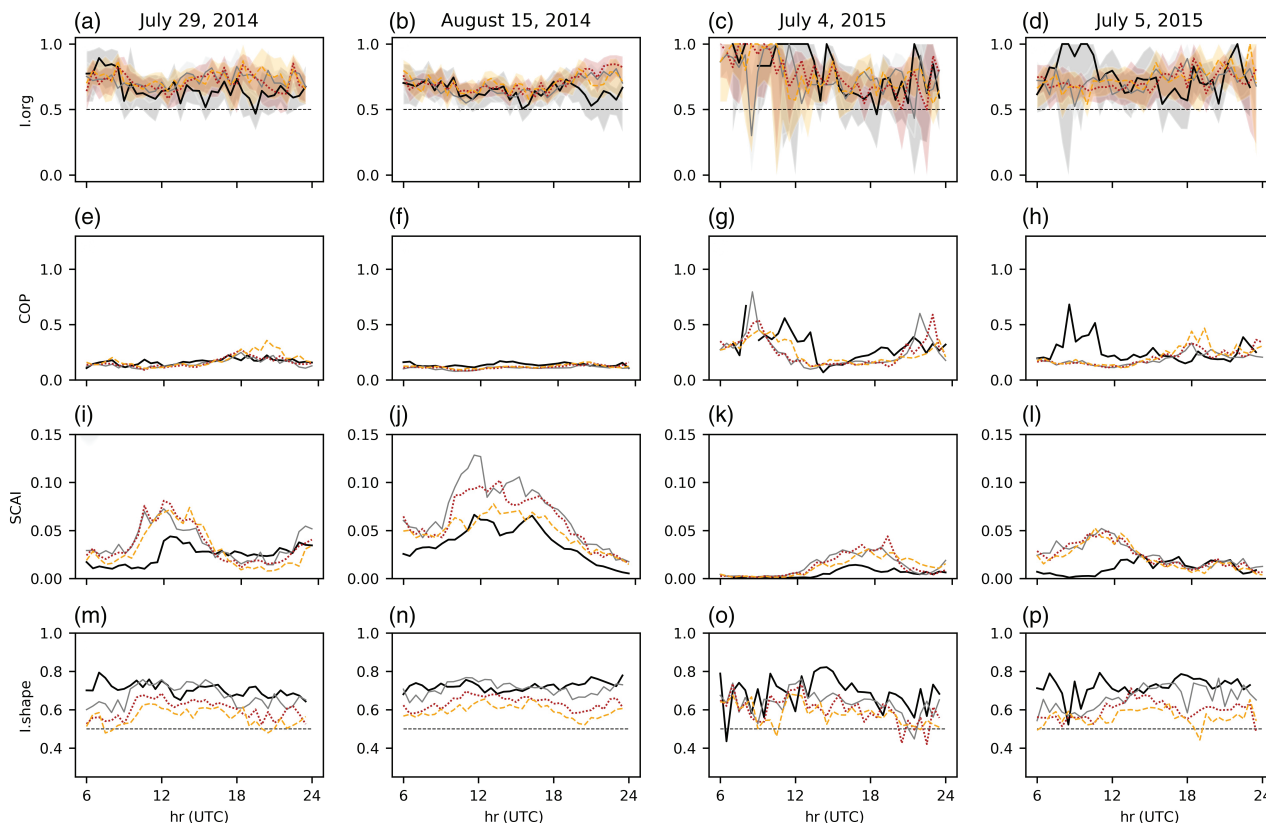
FIGURE 12   As Figure 11, but based on Meteosat and model-derived BTs

grid spacing of 625 m is closest to the observations, and as the grid spacing decreases the 2D shapes become more elongated.

This analysis also shows evidence that the combined use of the organization indices provides not only a better identification of the organizational state, but is also able to distinguish organization with fewer and larger objects (e.g. 4 and 5 July 2015) from organization with more and smaller objects (e.g. 29 July and 15 August 2014).

5 | SUMMARY AND CONCLUSIONS

To better understand convective organization and ultimately to enable the development of new parametrizations in climate prediction models, we performed this study to characterize convective organization over Germany. Object-based techniques have been applied to radar reflectivity and to infrared satellite imagery and different organization indices have been calculated for two extended summer seasons. Furthermore, large-eddy resolving simulations have been performed for selected days and their ability to represent convective organization has been evaluated. The impact of the employed grid spacings, varying between 625, 312, and 156 m has been investigated as well. Based on our analysis, we conclude the following:

1. Convection is organized most of the time over Germany, i.e. cloud tops and precipitation cores are organized for

69% and 92% of the analyzed time period, respectively. However, the organizational state of precipitation cores is difficult to assess from clouds tops, and *vice versa*. The 2D shapes tend towards a more elliptical shape for more organized distributions and vary between elliptical and circular otherwise.

2. Rainfall increase is associated with the increase in the number of objects and in object areas independent of the organizational state and is in agreement with Tobin *et al.* (2012), who also reported a correlation between the number of objects and precipitable water.

3. The number of objects and rainfall show a diurnal cycle, with noticeable increase after 1200 UTC, whereas there is no evidence of a diurnal cycle in the organizational state.

4. The large-eddy resolving simulations with grid spacings of 625, 312, and 156 m for the selected cases suffer from common biases that have been also experienced by others (Pearson *et al.*, 2014; Machado and Chaboureau, 2015; Rempel *et al.*, 2017; Senf *et al.*, 2018; White *et al.*, 2018): underestimation of rainfall, overestimation of cold cloud coverage and a too large number of small cloud tops and precipitation cores. However, the simulated organizational state is comparable to the observations, especially for precipitation cores. The 2D shape-based index I_{shape} shows the highest sensitivity to the grid spacing among the investigated indices. Shapes

of the cloud tops and precipitation cores derived from the simulations with 625 m grid spacing are closest to the observations, while finer resolutions lead to less realistic, too elliptic 2D shapes. On the other hand, there is also no improvement in the representation of rainfall rates and cloud top BTs through the decrease of the ICON grid spacing from 625 m down to 156 m, suggesting deficits in the applied mixed-phase and ice microphysics parametrization.

5. The use of a single organization index is not sufficient to fully characterize convective organization, since every index considers only a limited number of object characteristics. I_{org} is able to distinguish between organization, regular distribution and random distribution and is able to quantify this information for every single situation separately. Notwithstanding, it is challenging to identify further characteristics from it, such as object sizes and numbers. On the other hand, the latter are better represented in COP and SCAI, respectively, however COP and SCAI are not able to distinguish between the organizational states *per se*. Instead, they indicate if one situation is more or less organized than another one. They are therefore less suitable for the characterization of the organizational state of a single situation.

6. The combined use of I_{org}, COP and SCAI is able to distinguish organization with less numerous and larger objects from organization with more numerous and smaller objects in observations and simulations.

Since COP and SCAI have been found to be mostly influenced by the object areas and N, respectively, we recommend the joint use of I_{org}, I_{shape}, object areas and N for characterizing the organizational state of convection. This appears to be the most appropriate approach to investigate organization over a period of time as well as for the evaluation of model simulations. Although the use of observations from different instruments helps providing a more comprehensive characterization of organization, possible bias introduced due to distinct spatial resolutions of their measurements have not been considered in this study and is recommended for future investigations. As future work we also suggest the investigation of the temporal evolution of organization between radar and satellite observations as well as the characterization of radar objects based on the satellite-observed I_{org} organizational state, and *vice versa*. To elucidate the effect of convective organization on climate, further critical evaluations and a subsequent consolidation of indices for quantifying convective organizations is important as well.

ACKNOWLEDGEMENTS

REFERENCES

Baldauf, M., Seifert, A., Förstner, J., Majewski, D., Raschendorfer, M. and Reinhardt, T. (2011) Operational convective-scale numerical weather prediction with the COSMO model: description and sensitivities. *MWR*, 139(12), 3887–3905. https://doi.org/10.1175/MWR-D-10-05013.1.

Bartels, H., Weigl, E., Reich, T., Lang, P., Wagner, A., Kohler, O. and Gerlach, N. (2004) *Projekt RADOLAN – Routineverfahren zur Online-Aneichung der Radarniederschlagsdaten mit Hilfe von automatischen Bodennierderschlagsstationen (Ombrometer)*. Technical Report, Deutscher Wetterdienst, Offenbach, Germany

Benkrid, K. and Crookes, D. (2000) *Design and FPGA implementation of a perimeter estimator*. http://www.cs.qub.ac.uk/~d.crookes/webpubs/papers/perimeter.doc; accessed 6 May 2019

Bick, T. (2016) *3D radar reflectivity assimilation with an ensemble Kalman filter on the convective scale*. Dissertation, University of Bonn, Germany

Blahak, U. (2008) An approximation to the effective beam weighting function for scanning meteorological radars with axisymmetric antenna pattern. *Journal of Atmospheric and Oceanic Technology*, 25, 1182–1196.

Blahak, U., Zeng, Y. and Epperlein, D. (2011) Radar forward operator for data assimilation and model verification for the COSMO model. In proceedings of 35th AMS Conference on Radar Meteorology, Chicago, IL.

Bony, S., Stevens, B., Frierson, D.M.W., Jakob, C., Kageyama, M., Pincus, R., Shepherd, T.G., Sherwood, S., Siebesma, A., Sobel, A., Watanabe, M. and Webb, M. (2015) Clouds, circulation and climate sensitivity. *Nature Geoscience*, 8, 261–268. https://doi.org/10.1038/ngeo2398.

Bretherton, C.S., Blossey, P. and Khairoutdinov, M. (2005) An energy-balance analysis of deep convective self-aggregation above uniform SST. *Journal of the Atmospheric Sciences*, 62, 4273–4292.

Bretherton, C.S. (1988) A theory for nonprecipitating convection between two parallel plates, II, nonlinear theory and cloud field organization. *Journal of the Atmospheric Sciences*, 45(17), 2391–2415.

Brune, S., Kapp, F. and Friederichs, P. (2018) A wavelet-based analysis of convective organization in ICON large-eddy simulations. *Quarterly Journal of the Royal Meteorological Society*, 144, 2812–2829. https://doi.org/10.1002/qj.3409.

Cheng, W.-Y., Kim, D. and Rowe, A. (2018) Objective quantification of convective clustering observed during the AMIE/DYNAMO two-day rain episodes. *Journal of Geophysical Research: Atmospheres*, 123, 10361–10378. https://doi.org/10.1029/2018JD028497.

Dipankar, A., Stevens, B., Heinze, R., Moseley, C., Zängl, G., Giorgetta, M. and Brdar, S. (2015) Large-eddy simulation using the general circulation model ICON. *Journal of Advances in Modeling Earth Systems*, 7, 963–986. https://doi.org/10.1002/2015MS000431.

Duda, R.O. and Hart, P.E. (1973) Descriptions of line and shape. pp. 327–378 in *Pattern Analysis and scene analysis*, John Wiley and Sons, New York, NY.

DWD. (2018) RADOLAN/RADVOR: Hoch aufgelöste Niederschlagsanalyse und -vorhersage auf der Basis quantitativer Radar- und Ombrometerdaten für grenzüberschreitende Fluss-Einzugsgebiete von Deutschland im Echtzeitbetrieb. Technical Report version 2.4.4, Deutscher Wetterdienst, Offenbach, Germany

Hartmann, D., Hendon, H. and Houze, R.A. (1984) Some implications of the mesoscale circulations in tropical cloud clusters for large-scale dynamics and climate. *Journal of the Atmospheric Sciences*, 41(1), 113–121.

Heinze, R., Dipankar, A., Henken, C.C., Moseley, C., Sourdeval, O., Trömel, S., Xie, X., Adamidis, P., Ament, F., Baars, H., Barthlott, C., Behrendt, A., Blahak, U., Bley, S., Brdar, S., Brueck, M., Crewell, S., Deneke, H., Di Girolamo, P., Evaristo, R., Fischer, J., Frank, C., Friederichs, P., Göcke, T., Gorges, K., Hande, L., Hanke, M., Hansen, A., Hege, H.C., Hoose, C., Jahns, T., Kalthoff, N., Klocke, D., Kneifel, S., Knippertz, P., Kuhn, A., van Laar, T., Macke, A., Maurer, V., Mayer, B., Meyer, C.I., Muppa, S.K., Neggers, R.A.J., Orlandi, E., Pantillon, F., Pospichal, B., Röber, N., Scheck, L., Seifert, A., Seifert, P., Senf, F., Siligam, P., Simmer, C., Steinke, S., Stevens, B., Wapler, K., Weniger, M., Wulfmeyer, V., Zängl, G., Zhang, D. and Quaas, J. (2017) Large-eddy simulations over Germany using ICON: a comprehensive evaluation. *Quarterly Journal of the Royal Meteorological Society*, 143, 69–100. https://doi.org/10.1002/qj.2947.

Heise, E., Ritter, B. and Schrodin, E. (2006) *Operational implementation of the multilayer soil model TERRA*. COSMO Technical report 9. DWD, Offenbach, Germany. http://www.cosmo-model.org; accessed 6 May 2019

Holloway, C., Wing, A., Bony, S., Muller, C., Masunaga, H., L'Ecuyer, T., Turner, D. and Zuidema, P. (2017) Observing convective aggregation. *Surveys in Geophysics*, 38, 1199–1236. https://doi.org/10.1007/s10712-017-9419-1.

Holloway, C. and Woolnough, S. (2016) The sensitivity of convective aggregation to diabatic processes in idealized radiative-convective equilibrium simulations. *Journal of Advances in Modeling Earth Systems*, 8(1), 166–195. https://doi.org/10.1002/2015MS000511.

Houze, R.A. (1981) Cloud clusters and large-scale vertical motions in the Tropics. *Journal of the Meteorological Society of Japan*, 60(1), 396–409.

Houze, R.A. and Betts, A.K. (1981) Convection in GATE. *Reviews of Geophysical Research*, 19, 541–576.

Jerger, D. (2014) *Radar forward operator for verification of cloud-resolving simulations within the COSMO-model*. Dissertation, Karlsruhe Institute of Technology, Karlsruhe, Germany

Keil, C., Tafferner, A. and Reinhardt, T. (2006) Synthetic satellite imagery in the Lokal-Modell. *Atmospheric Research*, 82, 19–25. https://doi.org/10.1016/j.atmosres.2005.01.008.

Leuenberger, D., Koller, M., Fuhrer, O. and Schär, C. (2010) A generalization of the SLEVE vertical coordinate. *Monthly Weather Review*, 138, 3683–3689. https://doi.org/10.1175/2010MWR3307.1.

Lilly, D.K. (1962) On the numerical simulation of buoyant convection. *Tellus*, 14, 148–172. https://doi.org/10.1111/j.2153-3490.1962.tb00128.x.

Lo, C.P. (1980) Changes in the shapes of Chinese cities. *The Professional Geographer*, 32(2), 173–183.

Lopez, R. (1978) Internal structure and development processes of C-scale aggregates of cumulus clouds. *Monthly Weather Review*, 106, 1488–1494.

Louis, J.F. (1979) A parametric model of vertical eddy fluxes in the atmosphere. *Boundary-Layer Meteorology*, 17, 187–202. https://doi.org/10.1007/BF00117978.

Maceachren, A. (1985) Compactness of geographic shape: comparison and evaluation of measures. *Geografiska Annaler*, 67(1), 53–67.

Machado, L.A.T. and Chaboureau, J.P. (2015) Effect of turbulence parameterization on assessment of cloud organization. *Monthly Weather Review*, 143(8), 3246–3262. https://doi.org/10.1175/mwr-d-14-00393.1.

Mapes, B., Tulich, S., Lin, J. and Zuidema, P. (2006) The mesoscale convection life cycle: building block or prototype for large-scale tropical waves?. *Dynamics of Atmospheres and Oceans*, 42, 3–29.

McFarquhar, G.M., Iacobellis, S. and Somerville, R.C.J. (2003) SCm simulations of tropical ice clouds using observationally based parameterizations of microphysics. *Journal of Climate*, 16(11), 1643–1664. https://doi.org/10.1175/1520-0442(2003)016<1643:ssotic>2.0.co;2.

Mlawer, E.J., Taubman, S.J., Brown, P.D., Iacono, M.J. and Clough, S.A. (1997) Radiative transfer for inhomogeneous atmospheres: RRTM, a validated correlated-k model for the longwave. *Journal of Geophysical Research*, 102, 16663–16682. https://doi.org/10.1029/97JD00237.

Moncrieff, M.W. (2010) The multiscale organization of moist convection and the intersection of weather and climate. pp. 3–26 in *Climate Dynamics: Why Does Climate Vary?*, Sun, D.Z., Bryan, F. (eds), American Geophysical Union, Washington, D.C..

Moncrieff, M.W. and Liu, C. (2006) Representing convective organization in prediction models by a hybrid strategy. *Journal of the Atmospheric Sciences*, 63, 3404–3420. https://doi.org/10.1175/JAS3812.1.

Nair, U., Weger, R., Kuo, K. and Welch, R. (1998) Clustering, randomness, and regularity in cloud fields. 5. The nature of regular cumulus cloud fields. *Journal of Geophysical Research*, 103(D10), 11363–11380.

Nakajima, K. and Matsuno, T. (1988) Numerical experiments concerning the origin of cloud clusters in the tropical atmosphere. *Journal of the Meteorological Society of Japan*, 66(2), 309–329.

Pearson, K.J., Lister, G.M.S., Birch, C.E., Allan, R.P., Hogan, R.J. and Woolnough, S.J. (2014) Modelling the diurnal cycle of tropical convection across the 'grey zone'. *Quarterly Journal of the Royal Meteorological Society*, 140, 491–499. https://doi.org/10.1002/qj.2145.

Ramirez, J. and Bras, R. (1990) Clustered or regular cumulus clouds fields: the statistical character of observed and simulated cloud fields. *Journal of Geophysical Research*, 95(D3), 2035–2045.

Ramirez, J., Bras, R. and Emanuel, K. (1990) Stabilization functions of unforced cumulus clouds: their nature and components. *Journal of Geophysical Research*, 95(D3), 2047–2059.

Randall, D. and Huffman, G. (1980) Stochastic model of cumulus clumping. *Journal of the Atmospheric Sciences*, 37, 2068–2078.

Rempel, M., Senf, F. and Deneke, H. (2017) Object-based metrics for forecast verification of convective development with geostationary satellite data. *Monthly Weather Review*, 145(8), 3161–3178. https://doi.org/10.1175/MWR-D-16-0480.1.

Saunders, R., Matricardi, M. and Brunel, P. (1999) An improved for assimilation of satellite radiance observations. *Quarterly Journal of the Royal Meteorological Society*, 125, 1407–1425.

Schmetz, J., Pili, P., Tjemkes, S., Just, D., Kerkmann, J., Rota, S. and Ratier, A. (2002) An introduction to Meteosat Second Generation (MSG). *Bulletin of the American Meteorological Society*, 83(7), 977–992. https://doi.org/10.1175/BAMS-83-7-Schmetz-2.

Seifert, A. and Beheng, K.D. (2006) A two-moment cloud microphysics parameterization for mixed-phase clouds. Part 1: Model description. *Meteorology and Atmospheric Physics*, 92, 45–66. https://doi.org/10.1007/s00703-005-0112-4.

Seifert, A. and Heus, T. (2013) Large-eddy simulations of organized precipitating trade wind cumulus clouds. *Atmospheric Chemistry and Physics*, 13, 5631–5645. https://doi.org/10.5194/acp-13-5631-2013.

Senf, F. and Deneke, H. (2017) Uncertainties in synthetic Meteosat SEVIRI infrared brightness temperatures in the presence of cirrus clouds and implications for evaluation of cloud microphysics. *Atmospheric Research*, 183, 113–129.

Senf, F., Klocke, D. and Brueck, M. (2018) Size-resolved evaluation of simulated deep tropical convection. *Monthly Weather Review*, 146(7), 2161–2182.

Snedecor, G. and Cochran, W. (1989) *Statistical Methods*. (8th edition) Iowa State University Press, Iowa City, IA.

Tan, J., Jakob, C., Rossow, W.B. and Tselioudis, G. (2010) Increases in tropical rainfall driven by changes in frequency of organized deep convection. *Nature*, 519(7544), 451–454. https://doi.org/10.1038/nature14339.

Tobin, I., Bony, S. and Roca, R. (2012) Observational evidence for relationships between the degree of aggregation of deep convection, water vapor, surface fluxes, and radiation. *Journal of Climate*, 25, 6885–6904.

Tompkins, A. and Semie, A. (2017) Organization of tropical convection in low vertical wind shears: role of updraft entrainment. *Journal of Advances in Modeling Earth Systems*, 9, 1046–1068. https://doi.org/10.1002/2016MS000802.

Tselioudis, G., Tromeur, E., Rossow, W. and Zerefos, C. (2010) Decadal changes in tropical convection suggests effects on stratospheric water vapor. *Geophysical Research Letters*, 37(L14806), 1–4.

van Delden, A. and Oerlemans, J. (1982) Grouping of clouds in a numerical convection model. *Beitraege zur Physik der Atmosphaere*, 55(3), 239–252.

van der Walt, S., Schönberger, J.L., Nunez-Iglesias, J., Boulogne, F., Warner, J.D., Yager, N., Gouillart, E. and Yu, T. (2014) Scikit-image: Image Processing in Python, PeerJ 2:e453. https://doi.org/10.7717/peerj.453.

Wan, H., Giorgetta, M.A., Zängl, G., Restelli, M., Majewski, D., Bonaventura, L., Fröhlich, K., Reinert, D., Rpodas, P., Kornbluch, L. and Förstner, J. (2013) The ICON-1.2 hydrostatic atmospheric dynamical core on triangular grids – Part 1: formulation and performance of the baseline version. *Geoscientific Model Development*, 6, 735–763. https://doi.org/10.5194/gmd-6-735-2013.

Weger, R., Lee, J., Zhu, T. and Welch, R. (1992) Clustering, randomness and regularity in cloud fields: 1. theoretical considerations. *Journal of Geophysical Research*, 97(D18), 20519–20536.

Weigl, E. (2015) Radarniederschlag: Prinzip der Niederschlagsbestimmung mit Radar inkl. Umrechnung der Radarreflektivitäten in Momentanwerte des Niederschlages. Technical Report Version 1.1, Deutscher Wetterdienst, Offenbach, Germany

White, B.A., Buchanan, A.M., Birch, C.E., Stier, P. and Pearson, K.J. (2018) Quantifying the effects of horizontal grid length and parameterized convection on the degree of convective organization using a metric of potential for convective interaction. *Journal of the Atmospheric Sciences*, 75, 425–450. https://doi.org/10.1175/JAS-D-16-0307.1.

Wing, A.A. and Cronin, T. (2016) Self-aggregation of convection in long channel geometry. *Quarterly Journal of the Royal Meteorological Society*, 142, 1–15. https://doi.org/10.1002/qj.2628.

Wing, A.A., Emanuel, K.A., Holloway, C.E. and Muller, C. (2017) Convective self-aggregation in numerical simulations: a review. *Surveys in Geophysics*, 38, 1173–1197. https://doi.org/10.1007/s10712-017-9408-4.

Xia, L. (1996) Technical note. A method to improve classification with shape information. *International Journal of Remote Sensing*, 17(8), 1473–1481. https://doi.org/10.1080/01431169608948718.

Zängl, G., Reinert, D., Rpodas, P. and Baldauf, M. (2015) The ICON (ICOsahedral Non-hydrostatic) modelling framework of DWD and MPI-M: description of the non-hydrostatic dynamical core. *Quarterly Journal of the Royal Meteorological Society*, 141, 563–579. https://doi.org/10.1002/qj.2378.

Zeng, Y. (2013) *Efficient radar forward operator for operational data assimilation within the cosmo-model*. Dissertation, Karlsruhe Institute of Technology, Karlsruhe, Germany

Zeng, Y., Blahak, U. and Jerger, D. (2016) An efficient modular volume-scanning radar forward operator for NWP models: description and coupling to the COSMO model. *Quarterly Journal of the Royal Meteorological Society*, 142, 3234–3256. https://doi.org/10.1002/qj.2904.

Zhu, T., Lee, J., Weger, R. and Welch, R. (1992) Clustering, randomness, and regularity in cloud fields: 2. cumulus cloud fields. *Journal of Geophysical Research*, 97, 20537–20558. https://doi.org/10.1029/92JD02022.